Chemical Science

ROYAL SOCIETY OF CHEMISTRY

EDGE ARTICLE

View Article Online
View Journal | View Issue

Cite this: *Chem. Sci.*, 2025, **16**, 3560

All publication charges for this article have been paid for by the Royal Society of Chemistry

Electrochemically grafted molecular layers as on-chip energy storage molecular junctions†

Rajwinder Kaur,‡[a] Ankur Malik,‡[a] Ritu Gupta,[a] Kusum Kumari,[b] Saurabh Kumar Singh,[b] Paulo Roberto Bueno[c] and Prakash Chandra Mondal*[a]

Received 17th July 2024
Accepted 12th January 2025

DOI: 10.1039/d4sc04745a

rsc.li/chemical-science

Molecular junctions (MJs) are celebrated nanoelectronic devices for mimicking conventional electronic functions, including rectifiers, sensors, wires, switches, transistors, negative differential resistance, and memory, following an understanding of charge transport mechanisms. However, capacitive nanoscale molecular junctions are rarely seen. The present work describes electrochemically (E-Chem) grown covalently attached molecular thin films of 10, 14.3, and 18.6 nm thickness using benzimidazole (BENZ) diazonium salts on ITO electrodes on a quartz substrate upon which 50 nm of aluminum (Al) top contact was deposited to fabricate large-scale (area = 500 × 500 μm^2) molecular junctions. The capacitance of the molecular junctions decreases with increasing thickness of molecular layers, a behavior attributed to a classical dielectric role in which the geometric capacitance of the device within a uniform dielectric component is expected to decrease with increasing thickness. An electrical dipole moment in BENZ oligomers enhances polarizability; hence, the dielectric constant of the medium leads to an increase in the capacitance of MJs, which reaches a maximum value of ~53 $\mu F\ cm^{-2}$ for a junction of 10 nm molecular film thickness. In addition to direct-current (DC) electrical measurements, and computational studies, we performed alternating current (AC)-based electrical measurements to understand the frequency response of molecular junctions. Our present study demonstrates that BENZ-based molecular junctions behave as classical organic capacitors and could be a suitable building block for nanoscale on-chip energy storage devices.

Introduction

Existing complementary metal-oxide-semiconductor (CMOS) technology plays a crucial role in meeting the demand for compact and faster electronics. However, it is believed by many that microelectronics is about to reach the limit of miniaturization, which is constrained by physical principles.[1–4] Alternatively, molecular electronics (MEs) is an important platform and an attractive method compared to prevailing CMOS technology for next-generation micro to nanoelectronics. Molecular electronics, which deals with either a single molecule or a group of molecules sandwiched between two electrical conductors, either metallic or oxides, is considered a potential building block for diverse applications, including sensors, rectifiers, switches, and transistors. Molecular junctions have been studied by varying molecular structures, thickness, electrodes, molecular layer deposition methods, and current–voltage analysis techniques.[5–8] An external bias is applied to the two electrical contacts of molecular junctions, and the current–voltage (*I–V*) response is analyzed to design appropriate applications.[9–13] Charge transport through a single molecule, self-assembled monolayers (SAMs), oligomeric films or an electrochemically (E-Chem) grown method can mimic the electronic functions of traditional semiconductor devices, such as diodes,[7] transistors,[14] sensors and actuators,[15–17] switches,[18,19] spin transporting media,[20–22] and non-volatile memory, forming the basis for molecular electronics.[23–25] Considering the modern-day demand for high energy and power density energy storage devices, inorganic oxides have been extensively explored.[26–31] However, such materials require high processing temperatures, long reaction times to prepare, and high-vacuum deposition, which increase production costs. Additionally, the reproducibility of device yield remains in question as the bottom electrical contact utilizes mostly drop-casting, spin-coating, or physical vapor deposition methods, which create weaker electrode–material interfaces, and thus the devices may suffer from long-term stability problems. Instead, conductive

[a]*Department of Chemistry, Indian Institute of Technology Kanpur, Uttar Pradesh 208 016, India. E-mail: pcmondal@iitk.ac.in*

[b]*Department of Chemistry, Indian Institute of Technology Hyderabad, Kandi, Telangana 502 285, India*

[c]*Department of Engineering, Physics and Mathematics, Institute of Chemistry, Sao Paulo State University (UNESP), CEP 14800-060, Sao Paulo, Brazil*

† Electronic supplementary information (ESI) available. See DOI: https://doi.org/10.1039/d4sc04745a

‡ These two authors equally contributed to this work.

organic polymers, such as polyaniline (PANI) and polyaniline-tetracyanoquinodimethane (PANI-TCNQ) composite thin films, have been reported as good capacitors.[32–34] There is a consensus that organic molecules can offer several advantages over oxide materials due to their low-cost production and easy synthesis, tunable electrical conductivity, solution processability, light weight, flexibility, and the fact that they form covalent interfaces that are compatible with CMOS technology.[35–39] However, in pursuit of this goal, molecular junctions as "on-chip" capacitors have not been mechanistically explored, which could be due to the lack of a suitable molecular system design and device integration. A bottom-up approach in the fabrication of molecular electronic devices provides the advantage of controlling the thickness of molecular films within the junctions, thus altering their electronic properties as a function of thickness. Heteroatom (such as N, S, and O) doped and porphyrin-functionalized carbon materials have been proven to exhibit higher capacitance than undoped carbon materials due to their large difference in electronegativity, which causes an electrical dipole moment.[40–44] For instance, the McCreery group reports the presence of dielectric properties in tetraphenyl-porphyrin and fluorene-benzoic acid heterostructures, redox-active naphthalenediimide molecular layers placed between two conducting sp^2 carbon contacts and the effect of solvent vapor and mobile ions on capacitance.[45–47] The same group also developed nanoscale molecular films that could increase capacitance 100-fold compared to bare carbon electrodes, and capacitance studies were performed in acidic electrolytes.[48,49] In a recent report, around 1 nm thick benzo-15-*crown*-5-based SAM exhibited an areal capacitance of 3.68 μF cm^{-2}.[50] Typically, a classical capacitor utilizes two electrical conductors to separate the opposite charges using a dielectric component. However, all these demonstrations are limited to carbon electrodes fabricated *via* either electron-beam (e-beam) or pyrolyzed photoresist films (PPF), which are expensive and require a long time for electrode preparation.

Apart from electrode–molecule interfacial stability, E-Chem grafting and SAMs techniques offer advantages over drop-casting and spin-coating methods in terms of depositing molecular layers in a perpendicular orientation and controlling molecular layers on the substrate.[51,52] Physical methods such as drop casting and spin coating rely on non-covalent interactions (electrostatics, van der Waals forces) and non-uniform molecular structures. Hence, one might expect that a net dipole moment in the E-Chem-grafted molecular layers could preserve its structural integrity, and thus could be suitable for molecular capacitor applications. Molecular thin films possessing a net dipole moment can be electrochemically grafted on ITO substrates.[53]

We focus on fabricating heteroatom (nitrogen, sulfur)-containing molecular junctions that replace carbon electrodes as bottom contacts with technologically relevant ITO electrodes. An electrochemical (E-Chem) grafting method was employed to grow benzimidazole oligomer films, which is a much faster process than SAMs to grow molecular layers of varied thickness and is seemingly popular among other thin-film preparation strategies that use a covalent bond formation approach.[54–57] We chose aryl diazonium salts of 2-mercaptobenzimidazole, for which heteroatoms such as nitrogen–sulfur bonding can facilitate an increase in charge occupancy within spatial charge separation, which is so far an unexplored source of capacitance contribution in solid-state molecular junctions for 'on-chip' energy storage applications. Considering the experimental results, such as Mott–Schottky plots, VB-XPS, and thin film UV-vis spectroscopy, a proposed energy profile diagram is constructed.

Results and discussion

Heteroatom-containing imidazoles, due to their extended conjugation, play immensely important roles in tuneable properties; they are biologically relevant, as imidazoles are a constituent of active component vitamin B_{12} and DNA base structures.[58,59] The primary amino ($-NH_2$) group present in mercaptobenzimidazole can be diazotized (BENZ-D) using $NaNO_2$, which is a fast process, structurally confirmed *via* ^{1}H-NMR (Fig. S1, ESI†), FT-IR, and UV-vis spectra. A solution of 5-amino-2-mercaptobenzimidazole in dimethyl sulfoxide (DMSO) shows colorless, while diazonium salts exhibit an intense yellow color, confirming the formation of aryl diazonium salts (see the chemical structures in Fig. S2a†). The UV-vis spectrum of 5-amino-2-mercaptobenzimidazole in DMSO exhibits two intense peaks at 266, and 335 nm, due to π to π*, and n to π* electronic transitions, respectively (Fig. S2b†). The aryl diazonium chromophore exhibits absorption at 286 nm, which is around 20 nm red-shifted compared to that of the amine precursor. Additionally, it shows a broad band in the range of 350–535 nm, originating from a π to π* transition of the aromatic ring and an n to π* transition with λ_{max} at 413 nm, confirming the formation of the corresponding diazonium salts (see the normalized UV-vis spectra in Fig. S2b†), where the positive charge on the aryl ($Ar–N_2^+$) reduces the n to π* energy. The formation of the corresponding diazonium salts can be further confirmed by comparing the FT-IR spectra. The diazonium salts display vibrational stretching frequencies at 2560, 1620, 1460, and 1020 cm^{-1}, which are attributed to functional groups such as S–H stretching, C=C, C–H bending and B–F stretching, respectively (Fig. S2c†). A strong signal at 2250 cm^{-1}, which is absent in the amino precursor, confirms the formation of the aryl diazonium group. For the fabrication of MJs around 100 nm ± 5 nm thick and 500 μm wide, ITO electrodes were deposited on a freshly cleaned quartz substrate *via* reactive pulsed direct current magnetron sputtering using a custom-made shadow mask (details are provided in ESI, Fig. S3†).

An *ex situ* prepared diazonium salt solution (4 mM in dry acetonitrile) was electrochemically reduced to generate radicals on a chemically modified OH-terminated ITO electrode surface (as a working electrode in a three-electrode set-up) to produce strong, high-yield, fast-forming, robust covalent bonding between the molecule and the patterned ITO substrates. A proposed molecular layer structure is shown in Fig. 1a, for which we supported the structures with the help of spectroscopic and elemental characterization (see the discussion in the section below). Electrochemical (E-Chem) reduction of

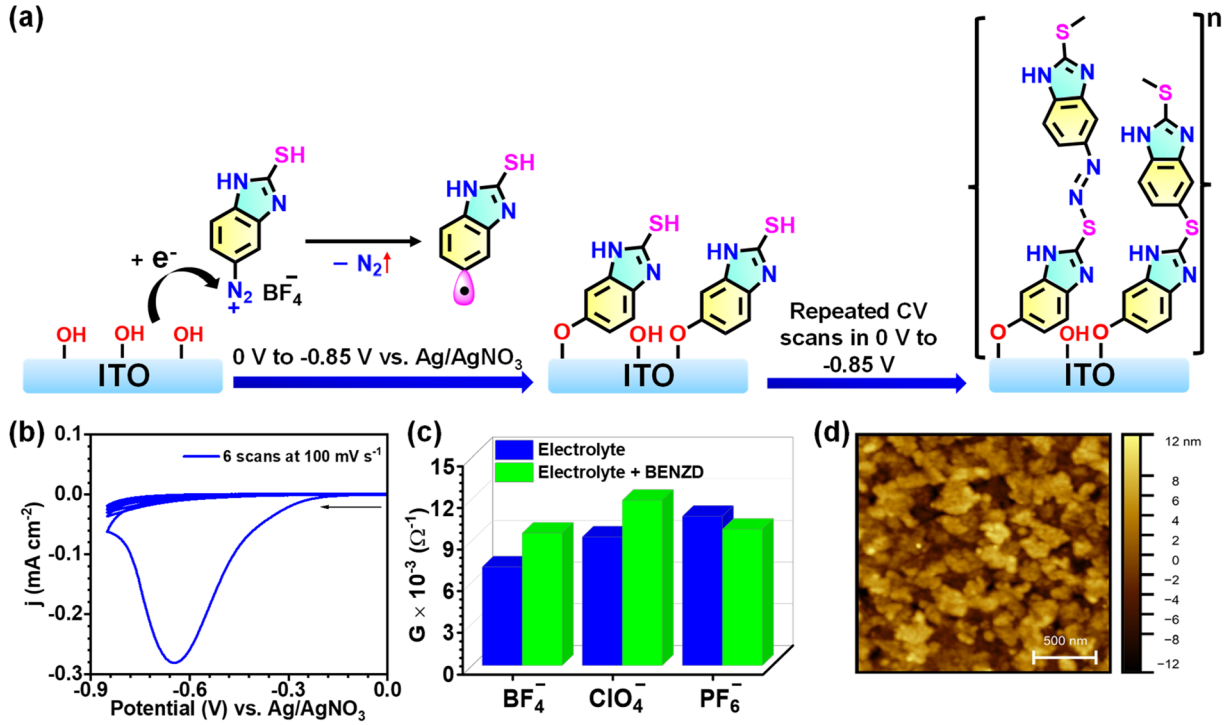

Fig. 1 Electrochemical grafting of 2-mercaptobenzimidazole diazonium salts on an ITO working electrode followed by characterization. (a) Schematic representation depicting the irreversible binding of benzimidazole molecular layers on the ITO electrode *via* a concerted mechanism employing the electrochemical reduction of diazonium salts. (b) Cyclic voltammogram manifesting the electrochemical reduction of BENZ-D on the ITO electrode with a prominent reduction peak at −0.65 V *vs.* $Ag/AgNO_3$ and the formation of a benzimidazole capacitive oligomeric film. (c) The impact of different electrolyte ions on the ionic conductance of the solution. (Blue and green bars represents the conductance of electrolyte ions alone and a mixture of electrolyte and BENZD.) (d) 2D AFM images of Film-1.

diazonium salt followed by thin-film formation was performed by sweeping the working electrode potential from 0 V to −0.85 V (*vs.* $Ag/AgNO_3$) for up to 6, 9, and 12 repetitive cyclic voltammogram (CV) scans recorded at a scan rate of 0.1 V s^{-1}, consequently forming Films 1, 2 and 3, respectively (Fig. 1b). A detailed discussion on electrochemical grafting is given in the ESI† (Section 4, E-Chem grafting CV for Film 1–3, Fig. S4a–c, and S5†). The voltammogram exhibits an aryl diazonium reduction peak, forming reactive radicals at −0.65 V, and it seems that most of the diazonium salts accessible near the ITO surface are consumed in film formation.[60] This E-Chem grafting process is so fast that in the 2nd CV scan, almost no prominent CV signal could be noticed, meaning that most of the diazonium salts near the electrode surface were reduced to form radicals. The surface coverage of Film-1 was estimated to be 6.1×10^{-9} mol cm^{-2}. The E-Chem conditions and a comparison of surface coverage for Films 1–3 are provided in the ESI (Table S1†) which are in good agreement with a well-packed molecular density on the ITO surface. As the surface coverage was calculated by integrating the area under the first CV scan in the case of Films 1–3, it is almost constant. In contrast, the increase in the number of CV scans from Film-1 to Film-3 resulted in increased thickness of the molecular films. As the oligomeric films are grown *via* aryl radicals, the possibility of branching molecular films cannot be ruled out, especially for thicker molecular layers.

Role of electrolyte ions on solution conductance and E-Chem grafting

For electrochemical cell reactions, electronic and ionic conductivity plays a crucial role. Electrolytes such as tetrabutylammonium tetrafluoroborate, tetrabutylammonium hexafluorophosphate, and tetrabutylammonium perchlorate, at 0.1 M concentration, are commonly employed as organic solvents to enhance the ionic conductivity of the solution. For our studies, we chose fluoroborate as a counter ion in benzimidazole diazonium salts, so $TBABF_4$ is the preferred electrolyte. The size and nature of electrolyte ions have an impact on the ionic conductivity, as evidenced by the electrochemical impedance spectra obtained for three different electrolytes (Fig. 1c, S6 and Table S2†). The order of ionic conductance is hexafluorophosphate > perchlorate > fluoroborate (Fig. 1c). However, in the presence of BEND salts, the order of ionic conductance is altered as follows: perchlorate > hexafluorophosphate > fluoroborate, which implies the different extent of interactions between BENZD and counter ions (Fig. 1c, S7 and Table S2†). To investigate the influence of ions on surface coverage, E-Chem grafting was performed under identical conditions utilizing three different electrolyte ions (Fig. S8†). BENZD perchlorate exhibits higher ionic conductance, which well matches the higher surface coverage observed. Ions that offer less resistance to the solution result in a higher degree of surface reactions and, hence, surface

coverage (Table S3†). The cyclic voltammogram of $TBABF_4$ under similar conditions utilized for E-Chem grafting of BENZD displays no characteristic electrochemical reduction peak (Fig. S9a†). However, the UV-vis spectrum of the ITO used for CV shows a broad absorption band at 412 nm, which might arise from electrolyte reduction at the electrode–electrolyte interface (Fig. S9b†). The intensity of the absorption band is quite low compared to BENZ film, implying that BENZD reduction during E-Chem grafting is the dominant reaction at the interface.

ITO/BENZ thin-film characterization

The morphology of Film-1 was analyzed using non-contact mode AFM, showing an increased roughness of 3.7 ± 0.2 nm (Fig. 1d). Such enhancement in roughness compared to the bare ITO (R_{rms} $\sim 2.8 \pm 0.2$ nm) is common for E-Chem-grafted molecular layers; hence, our findings confirm the formation of nanometric BENZ oligomers on ITO. The thicknesses of Films 1–3 were determined by scratching the molecular layers followed by atomic force microscopy measurements (details are given in the ESI section, Fig. S10 and S11†). Film-3 shows the greatest thickness of 18.6 ± 0.9 nm, which correlates well with the E-Chem grafting conditions, as it experiences more CV scans, and thus a longer time for consuming the maximum number of aryl radicals that take part in film formation.[61–63] The approximate number of benzimidazole units present in films of three different thicknesses, 10, 14.3, and 18.6 nm, were calculated from the length of the optimized structure of 4 BENZ units (Fig. S12 andTable S4†). The wettability measurements depict an increase in hydrophobicity after modification of the ITO surface with BENZ layers, which supports the formation of molecular thin films (Fig. S13 and Table S5†). A thin-film X-ray diffraction (XRD) pattern was recorded on a BENZ-modified ITO electrode, which exhibits peaks at 2 theta values of 30.34, 35.33, 50.73, and 60.38°, corresponding to the (222), (400), (441), and (622) planes of cubic indium tin oxides (JCPDS 00-039-1058), but whose intensities are reduced compared to those of bare ITO (Fig. S14†). As the films were grown *via* radical formation, which makes it difficult for them to grow and assemble in a specific pathway, PXRD suggests the amorphous nature of the oligomeric layers.

Absorption spectra of the films display a broad band in the wavelength range 360–600 nm with λ_{max} at 391 nm, demonstrating the formation of 2-mercapto benzimidazole films with the dominant feature of azo bridge (–N=N–) formation on ITO (Fig. S15a†). A rise in absorbance at 391 nm from Film-1 to Film-3 suggests an increase in the film thickness, but more random or sidewise growth of molecular films without much π-conjugation, as supported by the optical band gap values (Fig. S15b, and S16a–c†), which could most likely exist in the thinner films.[64,65] The optical band gap of ITO is 3.7 eV (Fig. S16d†). The azo groups (see the chemical structure in Fig. S5†) that are formed during E-Chem grafting facilitate lower energy electronic transitions (n to π*, and π to π*); thus there is a huge red shift of around 56 nm compared to the solution-phase spectra. Electrochemically grown BENZ thin films on an ITO substrate are thermally stable up to 150 °C, as supported by the thin-film UV-vis spectra (Fig. S17†). The ATR-IR spectrum after covalent modification of ITO with a BENZ layer displayed stretching vibrations at 1633 cm^{-1}, 1541 cm^{-1} (assigned to C=C), 1461 cm^{-1} (C=N), 3413 cm^{-1} with a shoulder band (N–H), 3121 cm^{-1} (aromatic C=C–H), and a band at 905 cm^{-1} (bending vibration, out-of-plane imidazole ring) characteristic of the benzimidazole ring present in the thin films. Such vibrations correlate well with a previous report.[66] Two additional stretching vibrations at 816 cm^{-1} and 2678 cm^{-1} correspond to the C–S–C linkage between the grafted molecules and the –SH moiety at the terminal end of E-Chem-grafted BENZ molecular layers. A weak-intensity band at 1323 cm^{-1} and a medium-intensity band of 654 cm^{-1} confirm the presence of an azo linkage and –S–N– bonds in the BENZ oligomeric films, respectively (Fig. S18†). Raman spectra obtained on BENZ-modified ITO showcased peaks at 622 cm^{-1}, 804 cm^{-1}, 967 cm^{-1}, 1402 cm^{-1}, 1454 cm^{-1}, 1554 cm^{-1}, and 1620 cm^{-1} corresponding to C–S, N–H, S–H, C–N, N=N, and C=C, respectively (Fig. S19, and Table S6†).[66–68] To diminish the photoluminescence effect, which causes a low signal-to-noise ratio in the case of ITO, BENZ-modified Au substrates were utilized for Raman spectroscopy studies, and characteristic Raman peaks were assigned according to previous reports in the literature.[66–68] Both thin-film FT-IR and Raman spectroscopy studies correlates well with each other and the bond vibration results combined with XPS analysis helped to deduce a plausible grafted film structure. The formation of such azo linkages (N=N) has been overlooked by many researchers in the domain of E-Chem-grafted thin films.

The deconvoluted X-ray photoelectron spectra (XPS) of constituent elements for bare ITO are presented in Fig. S20,† and that of Film-1 (~10 nm) is given in Fig. 2 and the results are summarized in Table S7.† The standard XPS signals of the constituent elements of bare ITO, *i.e.* $In5d_{5/2}$, $In5d_{3/2}$, $Sn5d_{5/2}$, and $Sn5d_{3/2}$, are observed at 444.18, 451.70, 486.29, and 494.77 eV, respectively.[69] The C1s peak can be fitted into six peaks at 284.2, 284.8, 285.43, 285.7, 286.17, and 287.00 eV for C=C, C–C/C–H, C=N, C–S, C–N, and C–O, respectively (Fig. 2a), which are well correlated with a previous report.[70] Nitrogen and sulfur are absent from the bare ITO sample, as expected, but clear XPS peaks of N1s and S2p are observed in the molecular films, which further confirm the film growth. The N1s peak can be further fitted into three peaks at 398.65, 400.40, and 402.24 eV, corresponding to azo (–N=N), pyrrolic-N, and pyridine-type nitrogen/N–S, respectively (Fig. 2b).[71] The O1s peak can be deconvoluted into four peaks at 529.78, 530.36, 531.14, and 532.09 eV, corresponding to oxygen in the oxide lattice with and without oxygen vacancies, O–H and C–O, which confirmed In/Sn–O–C bonding (Fig. 2c).[72,73] The S2p peak can be deconvoluted into two doublets: one at 164.25 eV (163.76 eV for $S2p_{3/2}$ and 164.84 eV for $S2p_{1/2}$) assigned to C–S and the other at 169.13 eV (168.54 eV for $S2p_{3/2}$ and 169.66 eV for $S2p_{1/2}$) assigned to N–S (Fig. 2d). Signals due to the presence of $In5d_{5/2}$, $In5d_{3/2}$, $Sn5d_{5/2}$, and $Sn5d_{3/2}$ are observed at BEs of 444.94, 452.48, 486.91, and 495.29 eV, respectively, with slightly higher binding energy than bare ITO (Fig. 2e and f).[74] Additionally, the intensity of O1s, In3d, and Sn3d in ITO-BENZ was significantly reduced compared to the films, due to the presence of other elements.

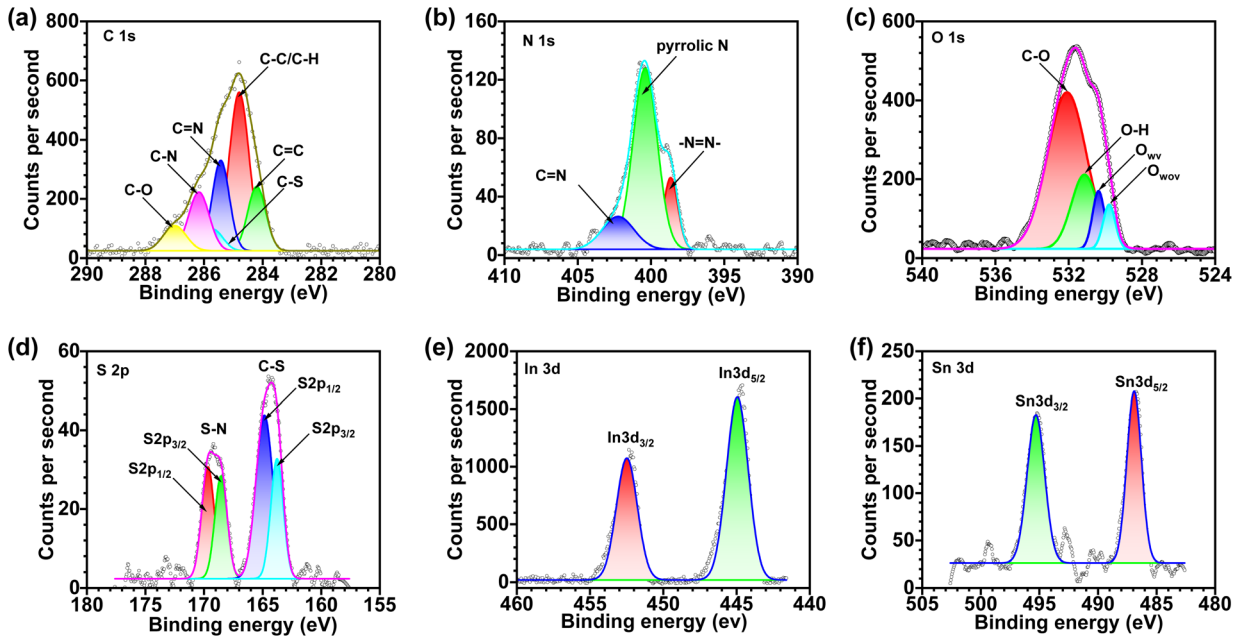

Fig. 2 High-resolution and deconvoluted XPS spectra of (a) C1s, (b) N1s (c) O1s, (d) S2p, (e) In3d, and (f) Sn3d of Film-1 that has been electrochemically grown on –OH-terminated ITO substrates. The characteristic signals related to the specific binding energy are marked in each spectrum.

Electrical characterization of ITO/BENZ/Al MJs

The two-terminal (2T) molecular junction structure and the side view of the sandwiched device are shown schematically in Fig. 3a. A detailed description of top contact deposition (Al, 50 nm thickness) is discussed in the ESI (Fig. S21a and b†). We considered ITO to be an important transparent conducting oxide electrode and molecular layers deposited on it could be suitable for optical, and optoelectronic studies. An Al top contact is cheaper than the widely used Au electrode. Two-probe electrical measurements of current *vs.* voltage characteristics (*I*–*V*) were performed on the freshly fabricated molecular junctions

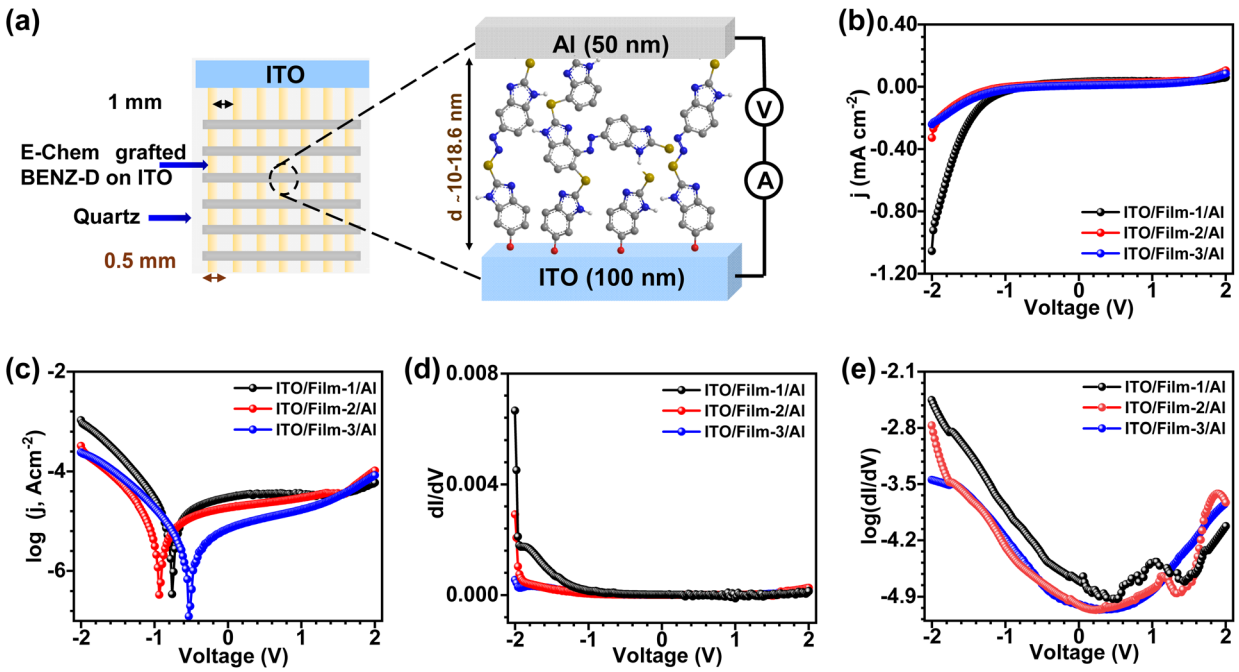

Fig. 3 Fabrication of ITO/BENZ/Al MJs of varying thicknesses followed by *I*–*V* characterization. (a) Illustration of ITO/BENZ/Al molecular junctions, and zoomed-in side view of an MJ. Comparison of (b) *j*–*V* plots, (c) log *j*–*V*, (d) d*I*/d*V* *vs.* *V*, and (e) log (d*I*/d*V*) *vs.* *V* plots of ITO/Film-1/Al to ITO/Film-3/Al MJs; *j* is the current density in Amp cm^{-2}.

(ITO/Film-1/Al, ITO/Film-2/Al, and ITO/Film-3/Al) with the measurement setup shown in Fig. S22.† In a controlled experiment, where junctions were fabricated without incorporating molecular layers, ITO/Al behaves as an ohmic conductor with a very high current density flowing in the circuit (Fig. S23a and b†). A comparison of electrical response (j = current density in mA cm^{-2}) in response to an applied bias range of ±2 V was made for all the molecular junctions (one-way, either 0 to +2 V or 0 to −2 V) (Fig. 3b–e). The average j–V curves in the ±2 V window for ITO/Film-1/Al, ITO/Film-2/Al, and ITO/Film-3/Al are shown in Fig. S24a–c.† The ITO/Film-1/Al MJs, composed of layers of 2-mercapto benzimidazole of around 10 nm, show a high current at both bias polarity and a rectification ratio (RR) of nearly 3, while ITO/Film-2/Al and ITO/Film-3/Al MJs show nearly symmetrical current–voltage responses. The junctions with thinner molecular layers most likely contain a strong interface effect and relatively more π-conjugation, which might cause the rectification.[7,75–77] Another interesting feature observed here is the non-zero current at 0 V, suggesting the charge-storage behavior of BENZ molecular layers (Fig. 3c). The magnitude of the non-zero current at 0 V decreases with an increase in layer thickness. The current density decreased with an increase in layer thickness,which is characteristic of tunneling molecular junctions.

A 1st derivative of current as a function of applied bias (dI/dV *vs.* V) helps us to understand the origin of the conductance in the devices. The ITO/Film-1/Al MJs show a sharp rise in conductance at −0.8 V due to the matching of the frontier molecular orbital of BENZ molecular layers and the Fermi energy of ITO, while no such rise in conductance is observed for thicker molecular films, such as ITO/Film-2/Al or ITO/Film-3/Al MJs (Fig. 3d and e).

Charge conduction in molecular junctions is contingent upon various factors, such as energy offset (the energy gap between the Fermi level of the electrode, E_F, and frontier molecular orbitals (FMO)), coupling strength, and the formation of gap states.[78,79] Depending on the position of the E_F of the electrode, the nature of the electrode–molecule electronic coupling and charge conduction mechanism can be altered.[80,81] For the experimental investigation, Hall measurements, Mott–Schottky analysis, and valence band XPS (VB-XPS) measurements were performed on bare ITO and ITO/Film-3. Hall effect studies demonstrate an increase in sheet resistance, and resistivity, and a decrease in carrier mobility for BENZ molecular films compared to bare ITO electrodes, confirming the attachment of molecular layers (Fig. S25 and Table S8†).[82] The sheet resistance is a good match to the resistance calculated from I–V measurements in the bias window of ±0.2 V (following Ohm's law in this region). The lower mobility, bulk, and surface concentration of charge carriers are observed in organic thin films, attributed to the localized charge carriers in localized molecular states.[83–85] The negative sign of the Hall coefficient signifies electrons to be the majority charge carriers in the molecular films (see Table S8†). Mott–Schottky plots obtained for bare ITO and ITO/Film-3 showed a positive slope at different frequencies, which points towards the n-type nature of the ITO and ITO/Film-3 system (Fig. S26a and b†).[86,87] The flat-band potential values obtained for bare ITO and ITO/Film-3 at 5 kHz, 1.5 kHz, 1 kHz, and 0.5 kHz using equations (i)–(iv) were used to determine conduction band minima (E_{CBM}) (Fig. S26c, d, Tables S9 and S10†).[88] The optical band gap combined with the E_{CBM} was used to obtain the valence band upper edge or valence band maximum value with reference to the vacuum level. The VB-XPS for bare ITO matches reports in the literature.[89] From the VB-XPS of bare ITO, the valence band maximum is 2.55 eV away from the Fermi level of the ITO electrode (Fig. S27a†). The VB-XPS for ITO/Film-3 displayed valence band onset ($E_F - E_{VBM}$) at 1.15 eV, which implies that the valence band lower edge is 1.15 eV away from the Fermi level of ITO/Film-3 and the conduction band lower edge is 0.67 eV away from the Fermi level of ITO/Film-3. The VB-XPS data exhibits the n-type nature of ITO/Film-3, as the Fermi energy level is closer to the conduction band of Film-3 (Fig. S27b†). Considering the E_F of ITO at −4.7 eV as per reports in the literature, the conduction band corresponding to the LUMO level of Film-3 is closer to the Fermi level of ITO and Al.[25] A plausible energy level diagram for the ITO/Film-3/Al MJs is shown in Fig. S28.† Hall measurements, Mott–Schottky plots, and VBXPS data correlate well with each other. Therefore, the LUMO of Film-3 is the dominant molecular orbital for charge conduction in ITO/Film-3/Al MJs. Carefully examining the optical band gap values in the case of 2, 3, and 4 units of BENZ layers obtained theoretically (6.45 eV), literature reports (4–5.2 eV),[80,90] and the experimental value of 1.82 eV suggests that, because of extended conjugation in multilayers of BENZ films, the HOMO and LUMO orbitals come closer to each other and the energy offset between the LUMO and the Fermi energy level of the electrode is decreased. This could be a plausible reason for the LUMO-controlled charge transport in ITO/BENZ/Al MJs.

The scan-rate-dependent I–V loop of the ITO/BENZ/Al junctions was examined under ambient conditions in the bias ranges of −1 to +1.5 V (Fig. S29†). With the increase in the scan rate, the enclosed area also continued to increase, suggesting an electrochemical capacitive contribution of the MJs (ITO/Film-1/Al MJs J–V hysteresis Fig. 4a). The calculated capacitances were 53.4 ± 13.5, 32.1 ± 7.48, and 26.8 ± 5.14 μF cm^{-2} for ITO/Film-1/Al, ITO/Film-2/Al, and ITO/Film-3/Al MJs, respectively, determined at a scan rate of 500 mV s^{-1} (Fig. 4b). The MJs exhibit classical capacitance, as the capacitance of the junctions was found to decrease with an increase in layer thickness, which acts here as a separator between two electrical conductors. The stability of the molecular junctions (ITO/Film-1/Al) was confirmed by running 3100 continuous j–V loops and it was reasonably stable with ∼95 ± 2% of initial capacitance retained after 1200 cycles and retention of ∼82 ± 2% of initial capacitance after 3100 cycles (Fig. 4c, and S30†). To understand the capacitance behavior of the BENZ imidazole-based nanoscale MJs, electrical impedance spectra (EIS) measurements were performed and the capacitance was demonstrated to be highly frequency dependent, a behavior that cannot be visualized from conventional direct current (DC)-based electrical measurements.[10] EIS studies were carried out on the molecular junctions at 100 mV amplitude applied between the bottom and top contacts. Such a high amplitude was chosen to obtain a high signal-to-noise ratio (S/N); however, it does not

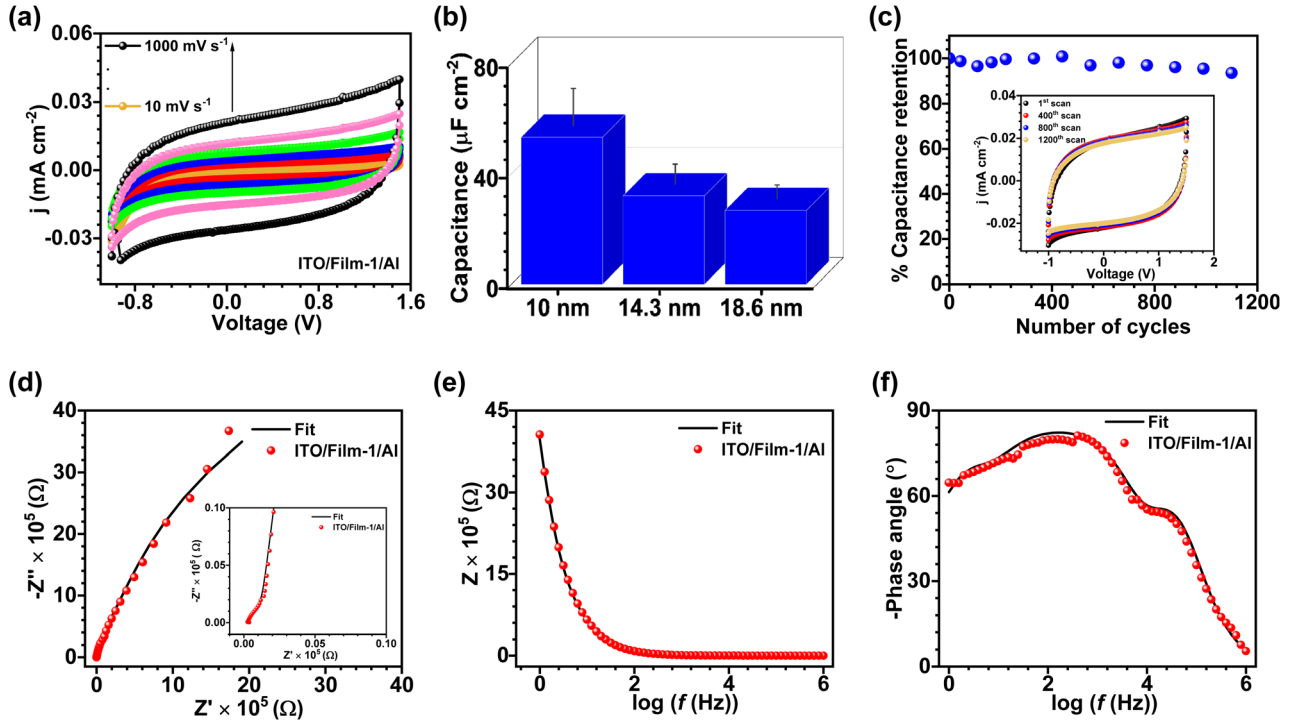

Fig. 4 DC and AC-based electrical measurements demonstrate the capacitive nature of molecular junctions. (a) Scan-rate-dependent J–V hysteresis in ITO/Film-1/Al MJs. (b) Bar plots with error bars for the variation in capacitance with the thickness of ITO/BENZ/Al MJs at 500 mV s^{-1}. (c) Capacitance retention in ITO/Film-1/Al MJs up to 1200 cycles. (d) Nyquist plot: Z'' (imaginary part) as a function of the real part Z' of the complex impedance of parallel plate capacitor. (e and f) Bode plot of ITO/Film-1/Al MJs measured at $V = 0$ DC voltage in the frequency range 10^6 to 1 Hz, applying AC perturbation of 100 mV amplitude.

hamper the linear response. The Nyquist plot, where Z' and Z'' indicate the real and imaginary parts of the complex impedance function, respectively, exhibits a steep line, which is typical capacitive behavior (Fig. 4d). The EIS data of the reference ITO/Al junction are provided in Fig. S31.† Additionally, a straight line in a low-frequency regime parallel to the imaginary y-axis confirms the capacitive nature of the junction. The impedance at higher frequency is related to R_u (contact resistance), which appears near the origin of the Nyquist plot, and the Bode plot shows a phase angle of ~6° at 1 MHz (note that the reference value is 0° for an ideal resistor). With decreasing frequency, capacitance starts to develop at the interfaces due to polarization of the molecular films. The capacitive reactance ($X_C = \frac{1}{j\omega CPE}$, where, $j = \sqrt{-1}$) increases with decreasing frequency. The Bode plot also shows a maximum phase angle of ~−82° at 158.4 Hz (note that the reference value is −90° for an ideal capacitor), which depicts the highly capacitive nature of ITO/Film-1/Al MJs at 158.4 Hz (Fig. 4e and f). At lower frequency, the capacitance reactance increases, so the current passes through the resistor, and the phase angle decreases (61° at 1 Hz).

An equivalent electrical circuit model comprising three resistances in parallel to the capacitance was used to evaluate the response of the MJs (Fig. S32, and Table S11†), where an uncompensated resistance (R_u) was considered in series to comprise the contact and other parasitic contact contributions. The three resistances in parallel with three capacitances correspond to the ITO/BENZ interface, BENZ layer, and BENZ/Al impedance, respectively. The capacitive reactance increases at higher frequencies; thus, the MJs behave as a resistor at frequencies over 10^3 Hz, and the phase angle also decreases as expected, in agreement with the equivalent circuit analysis. The EIS plots for ITO/Film-2/Al and ITO/Film-3/Al MJs are shown in Fig. S33.† The frequency-dependent capacitive response for the ITO/BENZ/Al MJs of different thicknesses is shown in Fig. S34.† The EIS data also shows a decline in capacitance with an increase in the thickness of the molecular film, a signature of classical molecular capacitors. The percentage device yield of fabricated MJs *via* the electrochemical grafting method is given in Table S12.† A comparison of fabricated ITO/BENZ/Al MJs to literature reports in terms of device performance demonstrates good capacitive features of ultrathin (10 nm) BENZ film. The fabricated devices require no binder, utilized in most capacitor devices, which makes ITO/BENZ/Al junctions light in weight. The performance is on the lower side compared to graphene-based micro-capacitors fabricated by sulfur heteroatom doping of graphene, which requires a high temperature of 800 °C, and expensive methods like the laser light scribing technique (Table S13†).[40,91]

Classical *vs.* quantum capacitance: a molecular approach

At the mesoscopic/nanoscopic electronic scale, it is well known that the circuit elements do not have the same physical interpretation as in the case of classic electronics.[92–94] The physical principles for electronic circuit elements at the nanoscale

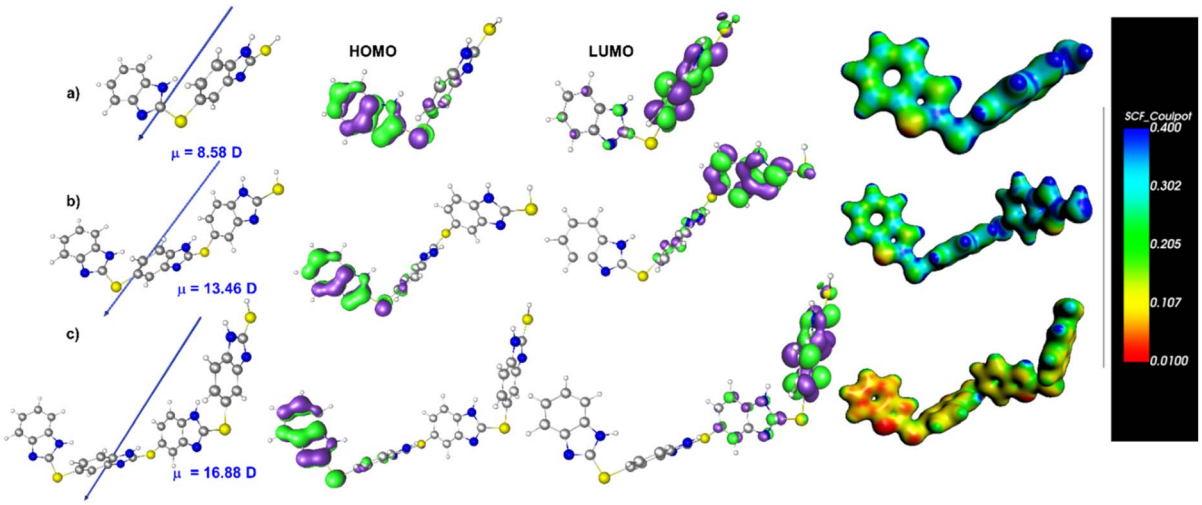

Fig. 5 DFT optimized geometry along with the calculated dipole moment, molecular orbital (MO) pictures, and the computed electrostatic potential maps for (a) 2, (b) 3, and (c) 4 units of benzimidazole.

depend on the electronic structure characteristics of nanoscale/molecular elements. For instance, the electrochemical capacitance C_μ is the series combination of spatial charge separation (associated with classical electric dipoles) C_e and electronic structure occupancy C_q contributions.[95] In an electrolyte environment nanoscale circuit, as is the case here, $C_e \sim C_\mu$, and the equivalent capacitance C_μ can be governed by $C_q \sim e(dn/dV)$ that, in turn, is dependent on the electronic structure that is macroscopically accessible by macroscopic contacts, where dn/dV is the electron occupancy n at given potential V. Notably, if electron occupancy n, which is volume dependent, increases with thickness, the capacitance can increase with thickness, which is not possible considering the classical characteristics of geometric C_e capacitance. In this way, molecular layers containing electronegative nitrogen and one sulfur-producing site in its structure that are accessible by macroscopic contacts can increase their capacitance if the number of molecular nitrogen–sulfur sites is increased. In other words, these types of sites can

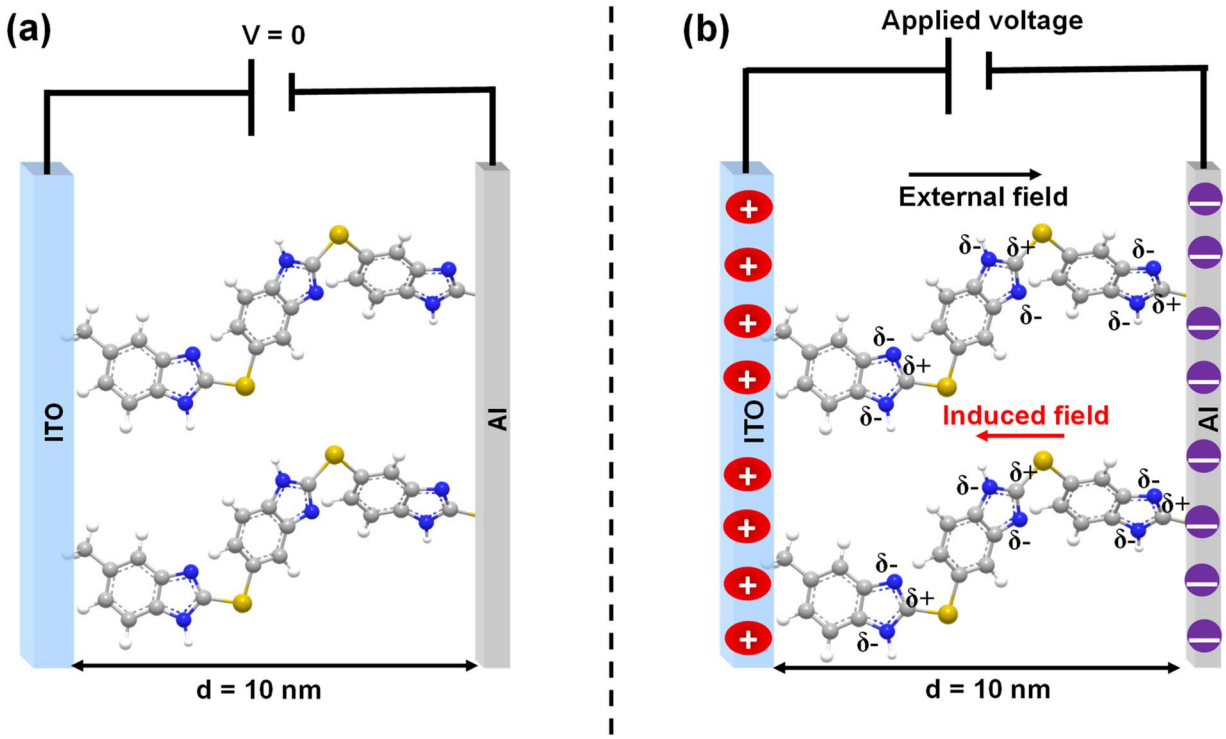

Fig. 6 A plausible charge storage mechanism in BENZ molecular films is proposed based on the mesoscopic physics of molecular junctions containing nitrogen–sulfur groups. (a) Schematic illustration of molecular layers in contact with two electrodes but in the absence of voltage; (b) electrochemical dipole-moment-driven electric field, and the presence of an external voltage.

be organized along with the size of the molecules and thus can be a source of capacitance that depends on layer thickness. A molecular occupancy of states, in the presence of an electrolyte, can act as an electrochemical type of dipole,[96] where the electron occupancy can be charge compensated by an ion in the free electrolyte, forming a nanoscale electron-ion-pair dipole.

In the present work, it has been observed that ITO/BENZ/Al MJs exhibit capacitive behavior. The emergence of capacitance in these MJs can be attributed to the significant amount of electrical dipole moment present in the heteroatom-containing benzimidazole molecules, as supported by the DFT calculations. Density functional theory (DFT) calculations were carried out at the B2PLYP level of theory[97] and aug-cc-pVTZ basis set to compute the dipole moments of 2, 3, and 4 units of optimized geometry of the BENZ molecular layers (see ESI for details†).[98] The DFT-computed dipole moments are 8.5 D, 13.5 D, and 16.9 D for 2, 3, and 4 units of BENZ molecular layers (Fig. 5a–c, and Table S14†). The observed increase in this type of electrical dipole moment with the rise in the number of molecular oligomeric layers could be the origin of the charge storage phenomenon in the molecular junctions, which is consistent with other types of high-magnitude capacitance observed in electrochemical environments, such as those associated with double-layer and pseudocapacitive phenomena. One might expect an increase in ITO/BENZ/Al MJs capacitance with an increase in the thickness of BENZ oligomeric thin film if electrochemical grafting occurs in a linear fashion. However, in our present study, the growth of oligomer layers of benzimidazole formed *via* reactive radicals is not fully linear, but rather is mixed with branched formation at higher thickness. The thin-film UV-visible results also support this argument. The BENZ layer acts as a dielectric medium and with an increase in the thickness of the layer, the capacitance value decreases, as in the case with classical capacitors.

The molecular layers have two subunits: (i) a less polarizable benzene ring and (ii) a highly polarizable imidazole ring, attached alternately in the E-Chem-grafted molecular thin films. At zero applied bias, the directions of polarizable units can be random and are averaged to produce a lower electrical dipole moment. To store charge within a good electric screen that is higher than the charge observed in pure macroscopic solid-state situations, a polarizable electrochemical subunit must have sufficient ability to contribute to the screening of the electric field in response to the applied external electric field coming from the macroscopic electrodes. In the presence of an external electric field, the BENZ layers with built-in permanent electrical dipole moments (due to the presence of heteroatoms) resulted in electrochemical dipolar-like polarization, which in turn contributed to the electric field screening and hence gave rise to higher capacitance in BENZ layers.[99,100] This is a plausible mechanism that is predicted by the mesoscopic physics of these MJs (Fig. 6).

Conclusions

Small-organic-molecule BENZ-based thin films display reasonable areal capacitance compared to inorganic-oxide-based nanometric dielectric films. To fabricate such molecular junctions, we employed an electrochemical grafting method to grow the molecular layers on a custom-made patterned ITO, producing a single chip of dimensions 15 mm × 15 mm, which can yield 30 molecular junctions in a time period which is highly advantageous for this method. The extent of polarizability or dipole moment present in oligomeric films of heteroatoms containing small organic molecules is a plausible reason for the higher capacitance observed. An ultrathin molecular film, according to classical physics or thickness-dependent polarization (as per quantum capacitance at the nanoscale) can give rise to higher capacitance. However, the experimental results were found to be inconsistent with the initial hypothesis of a rise in capacitance with increasing film thickness at the nanoscale. Considering an organic molecule as a single dipole, the orientation of dipoles is contingent upon the manner of film growth and the thickness of the film, and hence on the net electrical dipole moment of the films. The major disadvantage of the electrochemical grafting method is random and branched film growth. The branching in molecular film growth can reduce the net dipole moment of the film and hence the capacitance. Therefore, emphasis on molecular design to achieve linear film growth could provide a great opportunity to optimize thickness-dependent capacitance as well as the formation of pin-hole-free compact thin films. The electrochemical grafting technique deployed in this work can furnish ultrathin molecular films on versatile substrates, extending this approach to flexible electronics. On-chip charge storage in solid-state micro and nanoelectronics has always been challenging. The current study can inspire the development of a variety of heteroatom-containing molecular electronic devices for nanoelectronics applications, and open new avenues for exploring organic thin-film on-chip charge storage devices.

Data availability

All the data related to this work are available upon request to the corresponding author.

Author contributions

R. K.: device fabrication, electrical measurements, writing – original draft; A. M.: – synthesis of diazonium salts, thin film characterization, electrical characterization, analysis, writing the original, R. G.: thin film formation, and characterization, K. K.: DFT, and dipole moment calculation, S. S.: DFT, and dipole moment calculation, P. B.: quantum capacitance calculation, P. C. M.: investigation, supervision, writing, review & editing the original draft.

Conflicts of interest

No conflicts of interest to declare for this work.

Acknowledgements

R. K. and A. M. thank the University Grant Commission for a junior research fellowship (NTA Ref. No. 211610012732) and IIT

Kanpur for an Institute post-doctoral fellowship (PDF254) respectively. R. G. thanks to IIT Kanpur for the senior research fellowship. This work was financially supported by the Ministry of Education, Government of India for Scheme for Transformational and Advanced Research in Sciences (STARS) (Grant No. STARS-2/2023-0535), and the Science and Engineering Research Board (Grant No. CRG/2022/005325), New Delhi, India. The authors thank IIT Kanpur for the infrastructure and equipment facilities.

Notes and references

1 D. Karnaushenko, T. Kang, V. K. Bandari, F. Zhu and O. G. Schmidt, *Adv. Mater.*, 2020, **15**, 1902994.
2 Y. Zhao, M. Gobbi, L. E. Hueso and P. Samorì, *Chem. Rev.*, 2022, **122**, 50–131.
3 D. T. Simon, E. O. Gabrielsson, K. Tybrandt and M. Berggren, *Chem. Rev.*, 2016, **116**, 13009–13041.
4 J. Ma, S. Zheng, Y. Fu, X. Wang, J. Qin and Z.-S. Wu, *Chem. Sci.*, 2024, **15**, 5451–5481.
5 E. Gorenskaia and P. J. Low, *Chem. Sci.*, 2024, **15**, 9510–9556.
6 Z. Xie, I. Bâldea and C. D. Frisbie, *Chem. Sci.*, 2018, **9**, 4456–4467.
7 R. Gupta, J. A. Fereiro, A. Bayat, A. Pritam, M. Zharnikov and P. C. Mondal, *Nat. Rev. Chem*, 2023, **7**, 106–122.
8 H. Song, M. A. Reed and T. Lee, *Adv. Mater.*, 2011, **23**, 1583–1608.
9 X. Ding, J. Xue, S. Ding, C. Chen, X. Wang, X. Yu and W. Hu, *Angew. Chem., Int. Ed.*, 2022, **61**, e202208969.
10 P. Jash, R. K. Parashar, C. Fontanesi and P. C. Mondal, *Adv. Funct. Mater.*, 2022, **32**, 2109956.
11 B. Capozzi, J. Xia, O. Adak, E. J. Dell, Z. F. Liu, J. C. Taylor, J. B. Neaton, L. M. Campos and L. Venkataraman, *Nat. Nanotechnol.*, 2015, **10**, 522–527.
12 Z. Xie, I. Bâldea and C. D. Frisbie, *J. Am. Chem. Soc.*, 2019, **141**, 18182–18192.
13 S. Goswami, S. P. Rath, D. Thompson, S. Hedström, M. Annamalai, R. Pramanick, B. R. Ilic, S. Sarkar, S. Hooda, C. A. Nijhuis, J. Martin, R. S. Williams, S. Goswami and T. Venkatesan, *Nat. Nanotechnol.*, 2020, **15**, 380–389.
14 M. L. Perrin, E. Burzurí and H. S. J. Van Der Zant, *Chem. Soc. Rev.*, 2015, **44**, 902–919.
15 H. Atesci, V. Kaliginedi, J. A. Celis Gil, H. Ozawa, J. M. Thijssen, P. Broekmann, M. A. Haga and S. J. Van Der Molen, *Nat. Nanotechnol.*, 2018, **13**, 117–121.
16 S. K. Saxena, U. M. Tefashe, M. Supur and R. L. McCreery, *ACS Sens.*, 2021, **6**, 513–522.
17 U. Rashid, E. Chatir, L. Medrano Sandonas, P. Sreelakshmi, A. Dianat, R. Gutierrez, G. Cuniberti, S. Cobo and V. Kaliginedi, *Angew. Chem., Int. Ed.*, 2023, **135**, e202218767.
18 N. Darwish, A. C. Aragonès, T. Darwish, S. Ciampi and I. Díez-Pérez, *Nano Lett.*, 2014, **14**, 7064–7070.
19 T. Li, V. K. Bandari and O. G. Schmidt, *Adv. Mater.*, 2023, **35**, 2209088.
20 P. C. Mondal, C. Fontanesi, D. H. Waldeck and R. Naaman, *Acc. Chem. Res.*, 2016, **49**, 2560–2568.
21 C. Fontanesi, E. Capua, Y. Paltiel, D. H. Waldeck and R. Naaman, *Adv. Mater.*, 2018, **30**, 1707390.
22 K. Michaeli, D. N. Beratan, D. H. Waldeck and R. Naaman, *Proc. Natl. Acad. Sci. U. S. A.*, 2019, **116**, 5931–5936.
23 R. Gupta, P. Jash and P. C. Mondal, *J. Mater. Chem. C*, 2021, **9**, 11497–11516.
24 K. Terada, K. Kanaizuka, V. M. Iyer, M. Sannodo, S. Saito, K. Kobayashi and M. Haga, *Angew. Chem., Int. Ed.*, 2011, **123**, 6411–6415.
25 R. Gupta, S. Bhandari, S. Kaya, K. P. Katin and P. C. Mondal, *Nano Lett.*, 2023, **23**, 10998–11005.
26 S. K. Kim, S. W. Lee, J. H. Han, B. Lee, S. Han and C. S. Hwang, *Adv. Funct. Mater.*, 2010, **20**, 2989–3003.
27 J. Deng, X. Lu, L. Liu, L. Zhang and O. G. Schmidt, *Adv. Energy Mater.*, 2016, **6**, 1600797.
28 J. Han, F. Niroui, J. H. Lang and V. Bulović, *Nano Lett.*, 2022, **22**, 8258–8265.
29 M. Salanne, B. Rotenberg, K. Naoi, K. Kaneko, P. L. Taberna, C. P. Grey, B. Dunn and P. Simon, *Nat. Energy*, 2016, **1**, 1–10.
30 T. G. Yun, M. Park, D. H. Kim, D. Kim, J. Y. Cheong, J. G. Bae, S. M. Han and I. D. Kim, *ACS Nano*, 2019, **13**, 3141–3150.
31 Z. Song, G. Zhang, X. Deng, Y. Tian, X. Xiao, W. Deng, H. Hou, G. Zou and X. Ji, *Adv. Funct. Mater.*, 2022, **32**, 2205453.
32 D. Vonlanthen, P. Lazarev, K. A. See, F. Wudl and A. J. Heeger, *Adv. Mater.*, 2014, **26**, 5095–5100.
33 N. Dianat, M. S. Rahmanifar, A. Noori, M. F. El-Kady, X. Chang, R. B. Kaner and M. F. Mousavi, *Nano Lett.*, 2021, **21**, 9485–9493.
34 D. Q. Tan, *Adv. Funct. Mater.*, 2020, **30**, 1808567.
35 D. Xiang, X. Wang, C. Jia, T. Lee and X. Guo, *Chem. Rev.*, 2016, **116**, 4318–4440.
36 A. Vilan, D. Aswal and D. Cahen, *Chem. Rev.*, 2017, **117**, 4248–4286.
37 R. L. McCreery, *Acc. Chem. Res.*, 2022, **55**, 2766–2779.
38 E. M. Dief, P. J. Low, I. Díez-Pérez and N. Darwish, *Nat. Chem.*, 2023, **15**, 600–614.
39 R. K. Parashar, S. Kandpal, P. Bandyopadhyay, M. Sadhukhan, R. Kumar and P. C. Mondal, *Adv. Opt. Mater.*, 2023, **11**, 2202920.
40 Z. S. Wu, Y. Z. Tan, S. Zheng, S. Wang, K. Parvez, J. Qin, X. Shi, C. Sun, X. Bao, X. Feng and K. Müllen, *J. Am. Chem. Soc.*, 2017, **139**, 4506–4512.
41 S. Ghosh, S. Barg, S. M. Jeong and K. Ostrikov, *Adv. Energy Mater.*, 2020, **10**, 2001239.
42 H. Zhang, Y. Zhang, C. Gu and Y. Ma, *Adv. Energy Mater.*, 2015, **5**, 1402175.
43 M. Shahzad Khan, Q. Guo, W. Slough, A. Srivastava and R. Pandey, *Mater. Sci. Eng., B*, 2021, **272**, 115384.
44 Z. Zhang, X. Xu, X. Xing, X. Tang and X. Zhang, *Appl. Surf. Sci.*, 2025, **680**, 161327.
45 M. Supur, S. K. Saxena and R. L. McCreery, *J. Am. Chem. Soc.*, 2020, **142**, 11658–11662.
46 A. M. Najarian, M. Supur and R. L. McCreery, *J. Phys. Chem. C*, 2020, **124**, 1739–1748.

47 P. C. Mondal, U. M. Tefashe and R. L. McCreery, *J. Am. Chem. Soc.*, 2018, **140**, 7239–7247.
48 A. K. Farquhar, M. Supur, S. R. Smith, C. Van Dyck and R. L. McCreery, *Adv. Energy Mater.*, 2018, **8**, 1802439.
49 A. K. Farquhar, S. R. Smith, C. Van Dyck and R. L. McCreery, *ACS Appl. Mater. Interfaces*, 2020, **12**, 10211–10223.
50 S. C. Patrick, R. Hein, P. D. Beer and J. J. Davis, *Chem. Sci.*, 2024, **15**, 18310–18317.
51 Y. Pan, B. Tong, J. Shi, W. Zhao, J. Shen, J. Zhi and Y. Dong, *J. Phys. Chem. C*, 2010, **114**, 8040–8047.
52 W. Zhao, B. Tong, Y. Pan, J. Shen, J. Zhi, J. Shi and Y. Dong, *Langmuir*, 2009, **25**, 11796–11801.
53 S. Maldonado, T. J. Smith, R. D. Williams, S. Morin, E. Barton and K. J. Stevenson, *Langmuir*, 2006, **22**, 2884–2891.
54 R. Gupta, P. Jash, P. Sachan, A. Bayat, V. Singh and P. C. Mondal, *Angew. Chem., Int. Ed.*, 2021, **60**, 26904–26921.
55 P. Sachan and P. C. Mondal, *Analyst*, 2020, **145**, 1563–1582.
56 J. J. Gooding and S. Ciampi, *Chem. Soc. Rev.*, 2011, **40**, 2704.
57 R. Gupta, A. Malik, K. Kumari, S. K. Singh, V. Vivier and P. C. Mondal, *Chem. Sci.*, 2024, **15**, 8775–8785.
58 S. Suresh, K. Jayamoorthy, P. Saravanan and S. Karthikeyan, *Sens. Actuators, B*, 2016, **225**, 463–468.
59 S. A. M. Steinmueller, J. Fender, M. H. Deventer, A. Tutov, K. Lorenz, C. P. Stove, J. Hislop and M. Decker, *Angew. Chem., Int. Ed.*, 2023, **62**, e202306176.
60 R. Gupta, J. Pradhan, A. Haldar, C. Murapaka and P. C. Mondal, *Angew. Chem., Int. Ed.*, 2023, **62**, e202307458.
61 D. Bélanger and J. Pinson, *Chem. Soc. Rev.*, 2011, **40**, 3995–4048.
62 C. R. Peiris, Y. B. Vogel, A. P. Le Brun, A. C. Aragonès, M. L. Coote, I. Díez-Pérez, S. Ciampi and N. Darwish, *J. Am. Chem. Soc.*, 2019, **141**, 14788–14797.
63 J. C. Lacroix, *Curr. Opin. Electrochem.*, 2018, **7**, 153–160.
64 C. Van Dyck, A. J. Bergren, V. Mukundan, J. A. Fereiro and G. A. DiLabio, *Phys. Chem. Chem. Phys.*, 2019, **21**, 16762–16770.
65 S. Y. Sayed, J. A. Fereiro, H. Yan, R. L. McCreery and A. J. Bergren, *Proc. Natl. Acad. Sci. U. S. A.*, 2012, **109**, 11498–11503.
66 A. Suwaiyan, R. Zwarich and N. Baig, *J. Raman Spectrosc.*, 1990, **21**, 243–249.
67 J. Redolat, M. Camarena-Pérez, A. Griol, M. S. Lozano, M. I. Gómez-Gómez, J. E. Vázquez-Lozano, E. Miele, J. J. Baumberg, A. Martínez and E. Pinilla-Cienfuegos, *Nano Lett.*, 2024, **24**, 3670–3677.
68 Y. Chen, J. Yang, Z. Li, R. Li, W. Ruan, Z. Zhuang and B. Zhao, *Spectrochim. Acta, Part A*, 2016, **153**, 344–348.
69 P. C. Mondal, V. Singh, Y. L. Jeyachandran and M. Zharnikov, *ACS Appl. Mater. Interfaces*, 2015, **7**, 8677–8686.
70 M. Kasaeian, E. Ghasemi, B. Ramezanzadeh, M. Mahdavian and G. Bahlakeh, *Corros. Sci.*, 2018, **145**, 119–134.
71 M. Zhou, F. Pu, Z. Wang and S. Guan, *Carbon*, 2014, **68**, 185–194.
72 C. Zhang, L. Qi, Q. Chen, L. Lv, Y. Ning, Y. Hu, Y. Hou and F. Teng, *J. Mater. Chem. C*, 2014, **2**, 8715–8722.
73 D. Chen, C. Gan, X. Fan, L. Zhang, W. Li, M. Zhu and X. Quan, *Materials*, 2019, **12**, 2800.
74 C. Ruan, Q. Sun, D. Xiao, H. Li, G. Xia and S. Wang, *Ceram. Int.*, 2022, **48**, 12317–12323.
75 Z. Xie, I. Bâldea and C. D. Frisbie, *Chem. Sci.*, 2018, **9**, 4456–4467.
76 Y. An, M. Zhang, T. Wang, G. Wang and Z. Fu, *Phys. Lett. A*, 2016, **380**, 923–926.
77 J. Trasobares, D. Vuillaume, D. Théron and N. Clément, *Nat. Commun.*, 2016, **7**, 12850.
78 R. Kaur, B. Singh, V. Singh, M. Zharnikov and P. C. Mondal, *Coord. Chem. Rev.*, 2024, **514**, 215872.
79 C. P. Yu, S. Kumagai, T. Kushida, M. Mitani, C. Mitsui, H. Ishii, J. Takeya and T. Okamoto, *J. Am. Chem. Soc.*, 2022, **144**, 11159–11167.
80 O. Mahmoudi, T. Bordjiba and A. M. Affoune, *Int. J. Electrochem. Sci.*, 2016, **11**, 4427–4441.
81 E. Vernack, D. Costa, P. Tingaut and P. Marcus, *Corros. Sci.*, 2020, **174**, 108840.
82 J. S. Kim, F. Cacialli, A. Cola, G. Gigli and R. Cingolani, *Synth. Met.*, 2000, **111**, 363–367.
83 Y. Chen, H. T. Yi and V. Podzorov, *Phys. Rev. Appl.*, 2016, **5**, 034008.
84 H. T. Yi, Y. N. Gartstein and V. Podzorov, *Sci. Rep.*, 2016, **6**, 23650.
85 W. A. Wood, I. E. Jacobs, L. J. Spalek, Y. Huang, C. Chen, X. Ren and H. Sirringhaus, *Phys. Rev. Mater.*, 2023, **7**, 034603.
86 S. Saber, M. Mollar, A. El Nahrawy, N. Khattab, A. Eid, M. Abo-Aly and B. Marí, *Opt. Quantum Electron.*, 2018, **50**, 1–13.
87 K. Gelderman, L. Lee and S. W. Donne, *J. Chem. Educ.*, 2007, **84**, 685–688.
88 M. Gratzel, *nature*, 2001, **414**, 338–344.
89 V. Christou, M. Etchells, O. Renault, P. J. Dobson, O. V. Salata, G. Beamson and R. G. Egdell, *J. Appl. Phys.*, 2000, **88**, 5180–5187.
90 N. Kavitha, M. Alivelu and R. Konakanchi, *Polycyclic Aromat. Compd.*, 2022, **42**, 5534–5549.
91 Z. S. Wu, K. Parvez, X. Feng and K. Müllen, *Nat. Commun.*, 2013, **17**, 2487.
92 A. Santos, U. M. Tefashe, R. L. McCreery and P. R. Bueno, *Phys. Chem. Chem. Phys.*, 2020, **22**, 10828–10832.
93 F. A. Gutierrez, F. C. Bedatty Fernandes, G. A. Rivas and P. R. Bueno, *Phys. Chem. Chem. Phys.*, 2017, **19**, 6792–6806.
94 P. R. Bueno, T. A. Benites and J. J. Davis, *Sci. Rep.*, 2016, **6**, 18400.
95 P. R. Bueno, *Electrochim. Acta*, 2023, **466**, 142950.
96 E. F. Pinzón Nieto, E. V. G. Alarcón, Y. P. Sánchez and P. R. Bueno, *Phys. Chem. Chem. Phys.*, 2022, **24**, 16200–16206.
97 S. Grimme, *J. Chem. Phys.*, 2006, **124**, 034108.
98 A. L. Hickey and C. N. Rowley, *J. Phys. Chem. A*, 2014, **118**, 3678–3687.
99 L. Mourokh, C. Edder, W. Mack and P. Lazarev, *J. Mater. Sci. Appl.*, 2018, **09**, 517–525.
100 X. J. Liu, M. S. Zheng, G. Chen, Z. M. Dang and J. W. Zha, *Energy Environ. Sci.*, 2022, **15**, 56–81.